

# The Role of Chalcogen Vacancies in Single Photon Emission from Monolayer Tungsten Dichalcogenides

S. Carin Gavin,<sup>1,\*</sup> Charles J. Zeman IV,<sup>2,\*</sup> Anushka Dasgupta,<sup>3</sup> Yiyang Liu,<sup>1</sup> Wenjing Wu,<sup>4,5</sup> Shengxi Huang,<sup>4,5,6</sup> Tobin J. Marks,<sup>2,3,7,8</sup> Mark C. Hersam,<sup>2,3,8,9</sup> George C. Schatz,<sup>2</sup> and Nathaniel P. Stern<sup>1,†</sup>

<sup>1</sup>*Department of Physics and Astronomy, Northwestern University, Evanston, IL 60208, USA*

<sup>2</sup>*Department of Chemistry, Northwestern University, Evanston, IL 60208, USA*

<sup>3</sup>*Department of Materials Science and Engineering,  
Northwestern University, Evanston, IL 60208, USA*

<sup>4</sup>*Department of Electrical and Computer Engineering, Rice University, Houston, TX 77005, USA*

<sup>5</sup>*Smalley-Curl Institute, Rice University, Houston, TX 77005, USA*

<sup>6</sup>*Advanced Materials Institute, Rice University, Houston, TX 77005, USA*

<sup>7</sup>*Department of Chemical and Biological Engineering,  
Northwestern University, Evanston, IL 60208, USA*

<sup>8</sup>*Materials Research Center, Northwestern University, Evanston, IL 60208, USA*

<sup>9</sup>*Department of Electrical and Computer Engineering,  
Northwestern University, Evanston, IL 60208, USA*

Understanding the mechanism of single photon emission (SPE) in two-dimensional (2D) materials is an unsolved problem important for quantum optical materials and the development of quantum information applications. In 2D transition metal dichalcogenides (TMDs) such as tungsten diselenide (WSe<sub>2</sub>), quantum emission has been broadly attributed to exciton localization from atomic point defects, yet the precise microscopic picture is not fully understood. This work presents a new framework, supported by both computational and experimental evidence, to explain both the origins of facile SPE in WSe<sub>2</sub> and the relative scarcity of SPE in the related 2D TMD, tungsten disulfide (WS<sub>2</sub>). A vertical divacancy configuration of selenium creates a defect-centered, direct energy gap in the band structure of WSe<sub>2</sub>, giving rise to highly localized, radiative transitions. This configuration is shown to be energetically preferred in the monolayer lattice, which is reflected in the abundant experimental observation of SPE in WSe<sub>2</sub> both from the literature and this work. In contrast, the same vertical divacancy configuration in WS<sub>2</sub> does not create direct localized transitions, consistent with scarce observations of SPE in that material. By revealing a single mechanism in tungsten-based TMDs that addresses the prevalence of SPE and is consistent between theory and experiment, these results provide a framework for better understanding the rules governing the atomic origins of single photon emission in TMDs.

## I. INTRODUCTION

Single photon sources are critical to the field of quantum information processing. In recent years, single photon emission (SPE) from solid state materials such as carbon nanotubes, embedded quantum dots, and crystalline defects have collectively made advances as sources of quantum photons [1–3]. Two-dimensional (2D) materials such as transition metal dichalcogenides (TMDs) are an intriguing material host for SPE given their desirable coupling of optical properties with other degrees of freedom in areas such as valleytronics and spintronics [4, 5] and the emerging ability to tailor these properties via heterostructure engineering and surface modification [6, 7]. Therefore, understanding the microscopic origins of quantum emission in TMDs is key for controlling and customizing its use as an ingredient in quantum optical applications.

Within this class of materials, monolayer tungsten diselenide (WSe<sub>2</sub>) has been especially well-suited to the detection and control of SPE, with diverse and notable work dedicated to utilizing and understanding it [6–19]. The phenomenon has been broadly attributed to point defects within the 2D lattice that localize excitons [8–12]. Early reports of SPE in WSe<sub>2</sub> observed the characteristic sharp emission lines exclusively near creased edges of exfoliated flakes [8–10, 13], indicating the importance of mechanical strain in optically activating defect-bound transitions [12]. Consequently, arrays of quantum emitters can be generated deterministically with strain engineering [20–22]. Additionally, single photon electroluminescence in WSe<sub>2</sub> can be achieved with electrical pumping [16–19], which offers advantages for integrating quantum emission into devices. Yet, despite these abundant experimental observations of SPE in WSe<sub>2</sub> monolayers and heterostructures, its precise microscopic origins remain unclear. Theoretical models provide competing explanations regarding which atomic defects and conditions enable SPE [6, 23–28], and the variability of SPE phenomena across the TMD family complicates identi-

\* These authors contributed equally

† n-stern@northwestern.edu

fication of a single underlying mechanism that explains the full picture. Tungsten disulfide ( $\text{WS}_2$ ), molybdenum disulfide ( $\text{MoS}_2$ ), and molybdenum diselenide ( $\text{MoSe}_2$ ) all share the  $\text{MX}_2$  crystal structure and contain similar atomic defects and defect densities [29], yet while SPE in  $\text{WSe}_2$  is repeatedly observed under the simplest of defect and strain conditions, that from  $\text{WS}_2$ ,  $\text{MoS}_2$ , and  $\text{MoSe}_2$  is relatively scarce and requires specific and optimized defect and strain engineering techniques to manifest [30–35]. Altogether, there is no cohesive picture of the microscopic origin of SPE in TMDs that is consistent between theory and experiment and explains the observed discrepancies between the materials.

Our work addresses this discrepancy by interrogating the fundamental differences between selenium and sulfur vacancies and their effect on SPE formation between monolayer  $\text{WSe}_2$  and  $\text{WS}_2$ , both computationally and experimentally. The tungsten-based TMDs are isolated for comparison here because of their shared transition metal and dark state structure [25, 26, 36, 37]. This supports the assumption that the role of strain is consistent between materials and isolates the effect of the chalcogens as the variable being tested. By using density functional theory (DFT) calculations to compare the effect of various selenium and sulfur vacancy configurations on band structure, we show that only one selenium divacancy formation produces direct transitions between midgap defect states in  $\text{WSe}_2$ . Additionally, we show that this same divacancy is energetically preferred in the  $\text{WSe}_2$  lattice above all other modeled vacancy formations. Cryogenic optical measurements reveal that this divacancy translates to abundant, narrow linewidth SPE in monolayer  $\text{WSe}_2$ , consistent with prior reports. Conversely, all of the mono- and divacancy formations of sulfur create indirect midgap transitions in  $\text{WS}_2$ , demonstrated by its weak and broadened defect emission. Taken together, these models and measurements reveal that SPE in  $\text{WSe}_2$  originates from a naturally abundant, energetically preferred defect formation, which is reflected in the facile nature of experimentally observed SPE. Furthermore, this creates a framework to understand the fundamental differences between selenium and sulfur defects and their effect on single photon emission, which will help identify new methods to observe and utilize quantum emission in the TMDs.

## II. IDENTIFYING POINT DEFECT CANDIDATES

The vacancy configurations for modeling were chosen by determining relevant defect types and densities from the literature, with specific emphasis on the pertinent differences between  $\text{WSe}_2$  and  $\text{WS}_2$ . Monolayer TMDs, both exfoliated and grown by chemical vapor deposition, have typical defect densities of  $10^{12} - 10^{13} \text{ cm}^{-2}$  [38, 39].

This density is dominated by single chalcogen vacancies (monovacancies) from the top and bottom atomic planes of the  $\text{MX}_2$  crystal, indicated by the relatively low formation energy of monovacancies compared to transition metal defects or chalcogen multi-vacancies [29, 40, 41]. DFT analysis shows that chalcogen vacancies create localized midgap states close to the conduction band edge in  $\text{WSe}_2$  [6, 23, 24], suggesting that strain can optically activate dark defect states by lowering the conduction band edge so that it hybridizes with a midgap state [25, 26]. Given the reported abundance of monovacancies in all TMDs and their proposed role for SPE in  $\text{WSe}_2$ , they are an important defect type to model in a systematic investigation between  $\text{WSe}_2$  and  $\text{WS}_2$ .

Although single chalcogen vacancies are the dominant point defect, divacancies, consisting of two chalcogen vacancies in nearest neighbor sites, are also prevalent when defect density is high. Jeong *et al.* suggests that the relative likelihood of monovacancies to hybridize into divacancies is indicated by the single vacancy binding energy [42]. Where the single vacancy formation energy reveals the energetic cost of vacancy formation in a pristine lattice, the vacancy binding energy describes its thermodynamic stability within the lattice once created. Monovacancies with high binding energies are more likely to form divacancies in the lattice. Selenium monovacancies in  $\text{WSe}_2$  are shown to have  $\sim 2.5\times$  higher binding energy than sulfur monovacancies in  $\text{WS}_2$  [42], meaning that a higher proportion of them will be mutually attracted and hybridize into divacancies. The disparate prevalence of divacancies between the two tungsten-based TMDs is a key distinguishing feature and thus important for understanding contributions to SPE.

To systematically investigate defects as sources of SPE, we compare and contrast the band structures and localized states of monolayer  $\text{WSe}_2$  and  $\text{WS}_2$  resulting from six different vacancy geometries: monovacancies (configuration V1) and five nearest neighbor divacancies (configurations V2-V, V2-A, V2-B, V2-C, and V2-D), shown schematically in Figure 1. These geometries take into account all the symmetrical nearest neighbor sites of two chalcogens in the  $\text{MX}_2$  lattice.

It is crucial to note that DFT simulations reveal how energy levels of a monolayer semiconductor evolve when defects are introduced, which predicts whether defect-bound optical transitions are possible. However, they do not predict the specific energy of optical transitions. Additionally, DFT simulations do not reveal the quantum optical behavior of a single photon source directly. Rather, localized defect states induced by broken lattice symmetry are used as a proxy for predicting SPE [43]. Specifically, we will use the presence of allowed direct transitions between localized defect states to represent the conditions necessary for observing optical SPE that would be demonstrated by experimental quantum

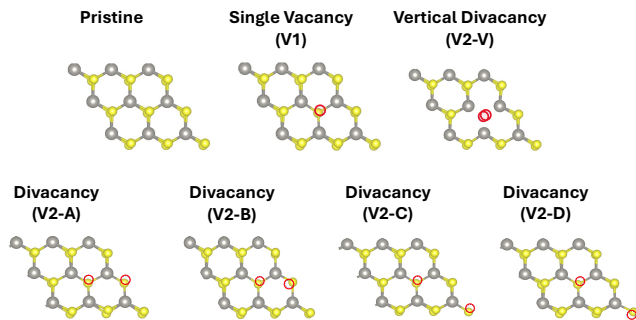


FIG. 1. Schematic of the pristine crystal and all modeled vacancy configurations: monovacancy (V1), vertical divacancy (V2-V), and divacancies V2-A, V2-B, V2-C, and V2-D. Chalcogen atoms are shown in yellow, while tungsten atoms are shown in grey.

statistics. This recognizes the importance of direct transitions for radiative recombination as well as the highly localized nature of SPE, and distinguishes candidate SPE from neutral and charged band edge excitonic emission. Although this simplified approach ignores complications such as excitation dynamics and strain activation that are important for experimental realization, it predicts the presence of candidate defect states that can be optically activated to emit as single photon sources.

### III. RESULTS

#### A. Modeling

The band structure of monolayer  $\text{WSe}_2$  and  $\text{WS}_2$  was modeled by DFT using the Heyd-Scuseria-Ernzerhof (HSE) functional [44]. This high level, range-corrected hybrid functional approximation was chosen to accurately predict localization of charges [45, 46], leading to more accurate defect state energy levels with respect to the valence band maximum (VBM) and conduction band minimum (CBM). The HSE band structure of pristine monolayers are shown in Figure 2b. A pristine  $3 \times 3$  supercell of both monolayer  $\text{WSe}_2$  (black) and  $\text{WS}_2$  (red) has a gamma-centered electronic structure that creates a direct bandgap between the CBM and VBM, indicated by the black arrow. This simple band structure is well-understood in modeling [47, 48], although experimental spectra exhibit complex emission lines due to the exciton fine structure [49]. Direct energy gaps are a critical feature of optical transitions because they facilitate fast rates of radiative decay, indicating their importance not only between band edges for excitonic emission, but between defect states for optical SPE as well.

Although single chalcogen vacancies (V1) are a popular candidate for SPE, our calculations show that they suppress direct optical transitions by introducing a com-

peting midgap state near the conduction band edge for both  $\text{WSe}_2$  and  $\text{WS}_2$  (Figure 2). This midgap state is degenerate except near the K-point, where a directional dependence emerges for the  $x$ - and  $y$ -oriented atomic orbitals ( $p_x$  and  $p_y$ ) (Figs. 2c,d). This occurs from the delocalization of electrons in the plane of the monolayer, facilitated by the hexagonal structure of covalently bonded tungsten and chalcogen atoms [50]. In other words, transitions involving the monovacancy midgap level are not highly localized. Additionally, the VBM creates an indirect gap with the defect level, precluding facile radiative decay from electrons that are excited to that defect state. Therefore, highly localized, optical SPE would not result from transitions involving the monovacancy-induced midgap levels for either  $\text{WSe}_2$  or  $\text{WS}_2$ .

The divacancy configurations V2-A, V2-B, V2-C, and V2-D also fail to create localized, optical transitions (Figs. 10,11 in Appendix C). All these configurations have two vacancies that are separated laterally in nearest neighbor corners of the hexagonal lattice. Divacancies in the supercell generally create two midgap states, an upper midgap level, dominated by  $p_x$  and  $p_y$  symmetry character, and the energetically lower  $p_z$  level. In these divacancy geometries, both midgap states are above the Fermi energy and are thus non-interacting. As such, the divacancies V2-A, V2-B, V2-C, and V2-D, have a similar effect to the monovacancy in that the midgap energy levels do not create direct transitions with either the VBM or the lower energy defect level, meaning highly localized SPE would not result from these defects.

In contrast, this effect is quite different for the V2-V divacancy. In this configuration, the nearest neighbor chalcogen vacancies are top-down (vertical) (Figure 3a), with the defect state primarily of  $p_z$  character. For the sulfur divacancy in  $\text{WS}_2$ , the resulting band structure is similar to the other divacancy configurations in which the  $p_z$  orbital is non-interacting (Figure 3c) because this state is energetically lower than the valence band. However, for the selenium divacancy in  $\text{WSe}_2$ , the highly localized defect state, indicated by its lack of curvature, has energy below the Fermi energy but above the VBM. The V2-V divacancy in  $\text{WSe}_2$  is distinguished from all other configurations in both materials by three crucial criteria. First, the two defect states are above and below the Fermi energy, meaning they can interact optically. Second, the transition between defect states induced by the vertical divacancy is highly localized to that defect, shown in the lack of curvature of the lower midgap level. Third, the lower defect band is K-centered along with the upper defect band, allowing a direct transition between defect states that would result in efficient optical recombination of highly localized emitters. This picture is supported by recent DFT-assisted calculations by Groll *et al.* that show charge density distribution modeling of a ‘selenium column’ in 2D  $\text{WSe}_2$ , which is

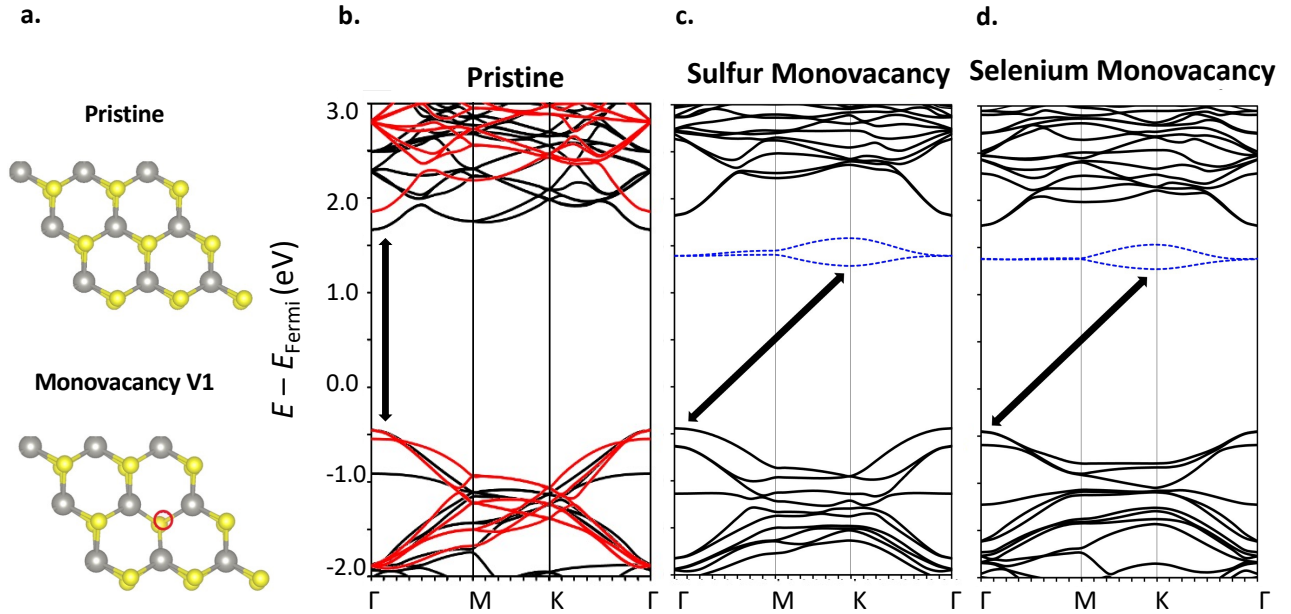


FIG. 2. (a) The lattice for a pristine TMD and the monovacancy (V1), where chalcogen atoms are shown in yellow and tungsten atoms are shown in grey. (b) Band structure of pristine monolayer WSe<sub>2</sub> (black) and WS<sub>2</sub> (red) showing the VBM and CBM aligned at the gamma point. Band structure of V1 in (c) WS<sub>2</sub> and (d) WSe<sub>2</sub>. Black arrows indicate the indirect alignment between defect state (dashed blue lines) and valence band edge.

equivalent to the V2-V vacancy geometry [51]. Charge density is localized in the region of the vertical divacancy from orbital hybridization, showing that the flat defect band arising from this unique geometry is indicative of localized transitions. The localized defect states and energy configuration that supports direct transitions is thus a key result for explaining SPE prevalence in WSe<sub>2</sub>, and it is at the same time missing in WS<sub>2</sub> divacancies as the lower energy vacancy level is buried below the VBM, providing an attractive explanation of the distinct behavior of these materials.

These calculations highlight the importance of vacancy configuration in predicting potential for SPE from defect band structure. For this prediction to be consistent with existing experimental observations, which show that SPE from WSe<sub>2</sub> is readily observed in typical monolayers, the optimum conditions for SPE should exist naturally in the WSe<sub>2</sub> lattice. To verify this, the formation energies of all modeled mono- and divacancy configurations of WSe<sub>2</sub> and WS<sub>2</sub> were calculated (Table I in Appendix C). The results reveal that the lowest formation energy belongs to single chalcogen vacancies for both WSe<sub>2</sub> ( $V_{1\text{Se}} = 2.98$  eV) and WS<sub>2</sub> ( $V_{1\text{S}} = 3.16$  eV), which is consistent with their proposed prominence in the literature. Additionally, the lowest divacancy formation energy for both monolayers belongs to the vertical divacancy V2-V for both WSe<sub>2</sub> and WS<sub>2</sub>. Looking specifically at the values for V1 and V2-V, these results show that vertical divacancies provide greater lattice stability than closely

spaced monovacancies in both WSe<sub>2</sub> and WS<sub>2</sub>. This is seen by considering twice the formation energy of a monovacancy in each material ( $2*V_{1\text{S}} = 6.31$  eV,  $2*V_{1\text{Se}} = 5.96$  eV) compared to the formation energy of vertical divacancies in each material ( $V2-V_{\text{S}} = 6.22$  eV,  $V2-V_{\text{Se}} = 5.54$  eV). The formation of two monovacancies is more energetically costly than the formation of a single vertical divacancy. This finding holds true in high defect density scenarios. For the 3x3 supercell used in this work, when a monovacancy is introduced within 4 atoms of an existing monovacancy, the configuration with the lowest formation energy is the vertical formation (V2-V). Not only is a divacancy less energetically costly than multiple monovacancies, but the specific V2-V divacancy is the least costly among all modeled vacancy configurations. This effect is more pronounced in WSe<sub>2</sub>, where the energy difference is -0.41 eV compared to WS<sub>2</sub> with an energy difference of -0.11 eV. This highlights the importance of local defect density fluctuations for forming SPE as opposed to the average large-scale density. Although an average vacancy density in TMDs may be on the order of  $10^{13}\text{cm}^{-2}$ , it is a locally higher density that facilitates optimal conditions for V2-V divacancies, and thus SPE. Altogether, this supports the idea that the V2-V vertical divacancy is the most energetically preferred and that WSe<sub>2</sub> is likely to have more monovacancies hybridize into divacancies for lattice stability than WS<sub>2</sub>. Most importantly, this specific V2-V formation uniquely creates direct, defect-centered optical transitions in the

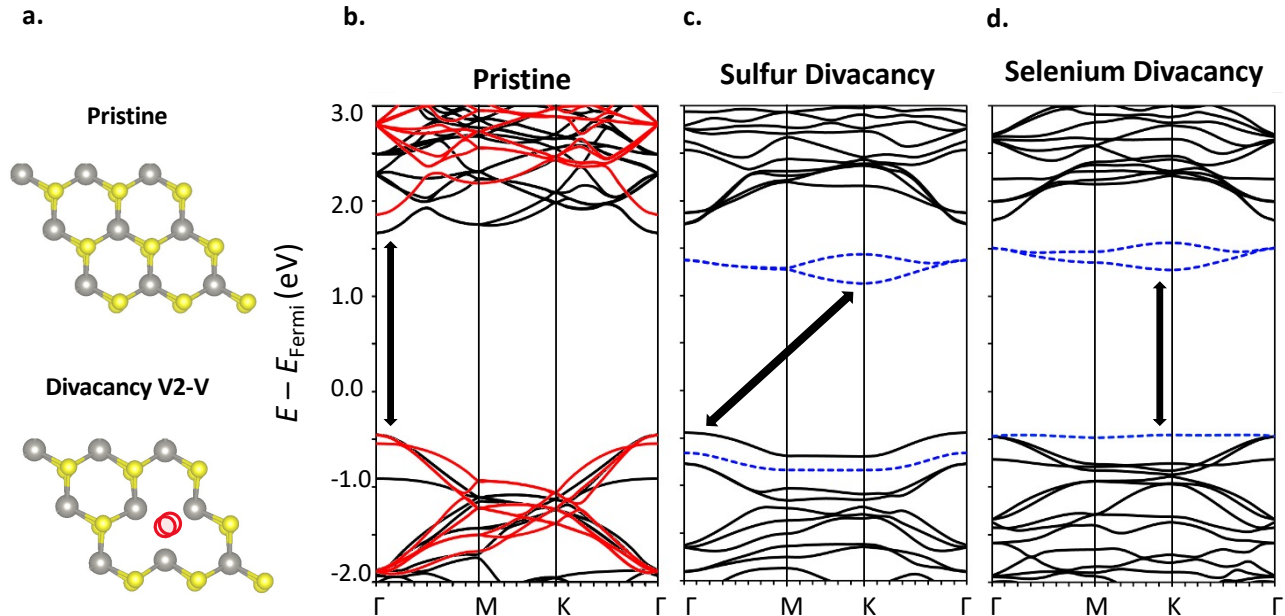


FIG. 3. (a) The lattice for a pristine TMD and the vertical divacancy (V2-V), where chalcogen atoms are shown in yellow, and tungsten atoms are shown in grey. (b) Band structure of pristine monolayer WSe<sub>2</sub> (black) and WS<sub>2</sub> (red) showing the VBM and CBM aligned at the gamma point. (c) The V2-V band structure in WS<sub>2</sub>. Black arrow indicates the indirect alignment between the defect state energy minimum (dashed blue line) and valence band edge, similar to the monovacancy. (d) The V2-V band structure in WSe<sub>2</sub>. Black arrow indicates the direct alignment between the upper and lower defect states (dashed blue lines).

band structure to yield highly localized optical SPE.

## B. Experiment

To verify these modeling insights, cryogenic optical spectroscopy was performed on both WSe<sub>2</sub> and WS<sub>2</sub> monolayers that were prepared under the same conditions. The modeling predicts that the V2-V divacancy is energetically favorable and creates defect-centered transitions in WSe<sub>2</sub>. If these metrics are effective proxies for quantum emission, SPE should be readily observable from typical WSe<sub>2</sub> monolayers. To confirm this, photoluminescence (PL) mapping was first performed on monolayer WSe<sub>2</sub> at a temperature of  $T = 1.6$  K. Cryogenic temperatures, ideally below 10 K, are necessary for observing SPE in TMDs because of the low binding energies of defect-bound excitons [52, 53]. Consistent with early reports [8], emission from the neutral exciton is shown to be comparable across the entire monolayer area (Figure 4d), whereas defect-bound emission is intense on edges and areas of strain (Figure 4e).

A selected low energy, localized emitter is shown in the blue spectrum of (Figure 4c,f) and is identified as a SPE source by measurement of the second-order photon correlation  $g^{(2)}(\tau)$  (Figure 4f, inset). To extract a normalized  $g^{(2)}(0)$  value, the data is fit so that the large  $\tau$  value

corresponding to coherent light is equal to one. Finding that  $g^{(2)}(0) < 0.5$  confirms this is a single photon source. Atomic force microscopy identifies strain manifesting as microscopic cracks and wrinkles (Figure 4b), with locations of strain corresponding to locations of SPE (Figure 4e). Further SPE in this sample was identified and characterized (see Appendix Figure 9).

Next, PL mapping was performed on monolayer WS<sub>2</sub> under the same conditions, shown in Figure 5. The intensity of the peak attributed to the neutral exciton is similar across the monolayer area as it is in WSe<sub>2</sub> (Fig. 5d). However, unlike WSe<sub>2</sub>, the WS<sub>2</sub> sample does not show localized emission near flake edges or in strained regions (Figure 5e). While the spectral map shows there is some variation in total PL intensity across the sample, the individual spectra (Figure 5c) show that this is the result of the WS<sub>2</sub> trion at 609 nm [54, 55], which varies around 40% in maximum peak intensity, rather than defect-mediated SPE. Spectra are collected from areas of the flake with different morphology (a smooth region, a crease, and an edge) to assess the effect of strain. As seen in Figure 5f, the highly strained crease area shows enhanced defect emission intensity. Yet unlike WSe<sub>2</sub>, which exhibits quantum emission far below ( $\sim 220$  meV) the neutral exciton energy, emission below the excitonic complex energy in WS<sub>2</sub> remains broad and weak. This is consistent with the interpretation from our

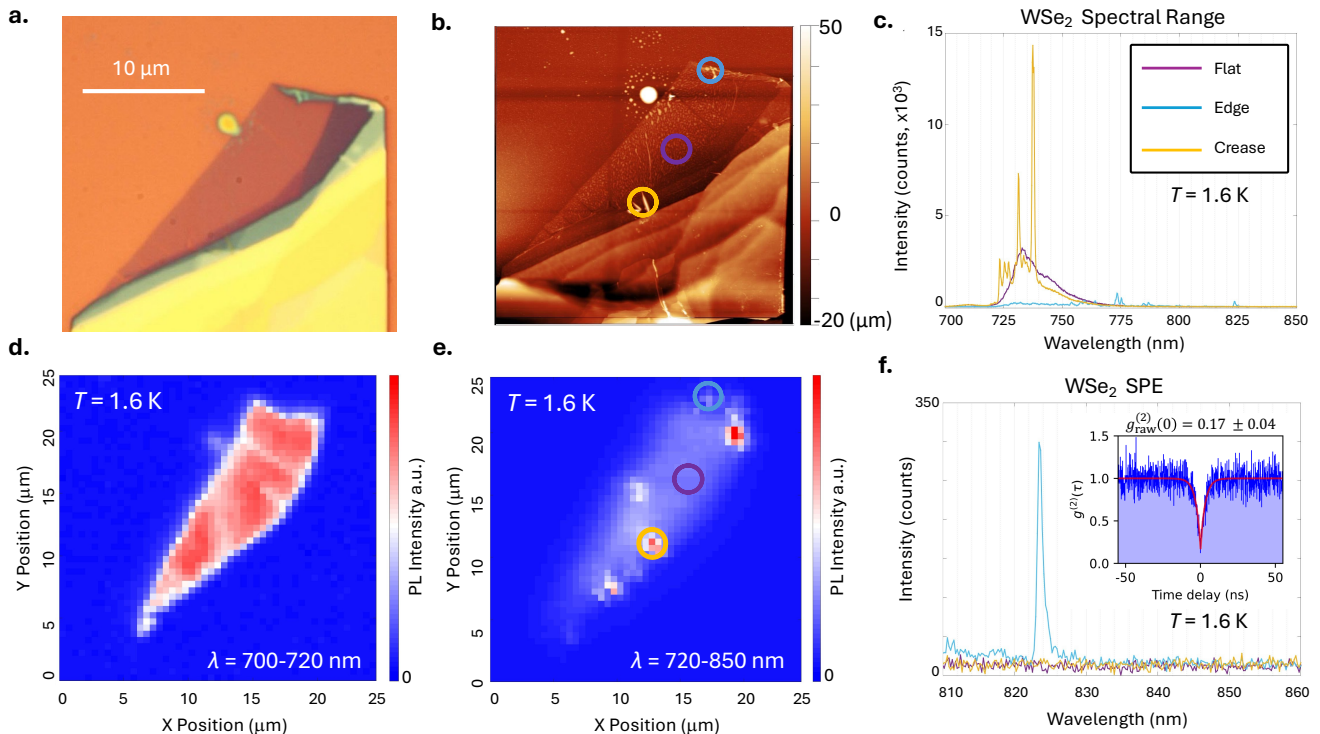


FIG. 4. (a) Optical microscope image of WSe<sub>2</sub> monolayer. (b) Atomic force microscopy (AFM) image of the WSe<sub>2</sub> monolayer with areas circled corresponding to smooth (purple), creased (orange), and edge (blue). (c) Low-temperature emission spectra from regions of WSe<sub>2</sub> identified in AFM image. Strained areas exhibit narrow, localized emission features. (d) Map of monolayer emission integrated over the neutral exciton range (700 – 720 nm), showing the uniform intensity of exciton emission across the flake. (e) Map of monolayer emission integrated over wavelengths beyond the neutral exciton (> 720 nm), showing localized, preferential emission near edges, folds, and cracks as identified with AFM. (f) Localized emission feature from the edge strained (blue) spectrum in (c). Inset shows the characteristic antibunching behavior of a single photon emitter in  $g^{(2)}(\tau)$  with  $g^{(2)}(0) = 0.17$ .

DFT modeling, which predicts that both sulfur mono- and divacancies will create broadened defect emission rather than highly localized SPE because they are intrinsically indirect transitions. It is also consistent with prior reports of broad defect emission bands (L-bands) in the sulfur TMDs [33, 49, 56], which are attributed to both sulfur vacancies and accumulation of adsorbates into those sites.

These measurements compare the low-T optical properties of WSe<sub>2</sub> and WS<sub>2</sub> under as-exfoliated conditions, with no intentional defect or strain engineering. The observations are consistent with an explanation based on formation energies and direct optical transitions in SPE proxies from DFT. However, measurement of ‘typical’ WS<sub>2</sub> does not robustly explore the impact of divacancies since they are less energetically favorable than in WSe<sub>2</sub>. For completeness, it is desirable to observe the effect of divacancies in WS<sub>2</sub> directly. To achieve this, a WS<sub>2</sub> monolayer was defect-engineered to enhance divacancy density by bombarding it with argon plasma using plasma-enhanced atomic layer deposition [33, 57]. The plasma bombardment ejects sulfur atoms from the lat-

tice, engineering a significant increase in vacancy density. Sulfur single and di-vacancies were confirmed using scanning transmission electron microscopy (STEM) imaging [57]. An average defect density of approximately  $10^{14}$  cm<sup>-2</sup> was determined for this new material (Ar-WS<sub>2</sub>), an order of magnitude greater than typical in pristine samples [38, 39].

Optically, Ar-WS<sub>2</sub> exhibits a weak, red-shifted exciton emission compared to pristine WS<sub>2</sub> and a new broad low-energy emission feature, likely due to new defects (Fig. 6). The typical L-band of WS<sub>2</sub>, centered around 670 nm [58], is clearly evident in the pristine monolayer (Figure 6a), which can be characterized by a single Gaussian peak centered at 669 nm. In Ar-WS<sub>2</sub>, there is an intense defect peak analogous to this L-band, but the full spectral range cannot be convincingly fit by a single Gaussian due to a low-energy tail (Figure 6b). This new low-energy emission, which is only observed in Ar-WS<sub>2</sub>, may result from the increased divacancy density. In summary, a monolayer of typical defect density in WS<sub>2</sub> is characterized by the L-band as described in the literature, and this L-band remains when the WS<sub>2</sub> is engineered to

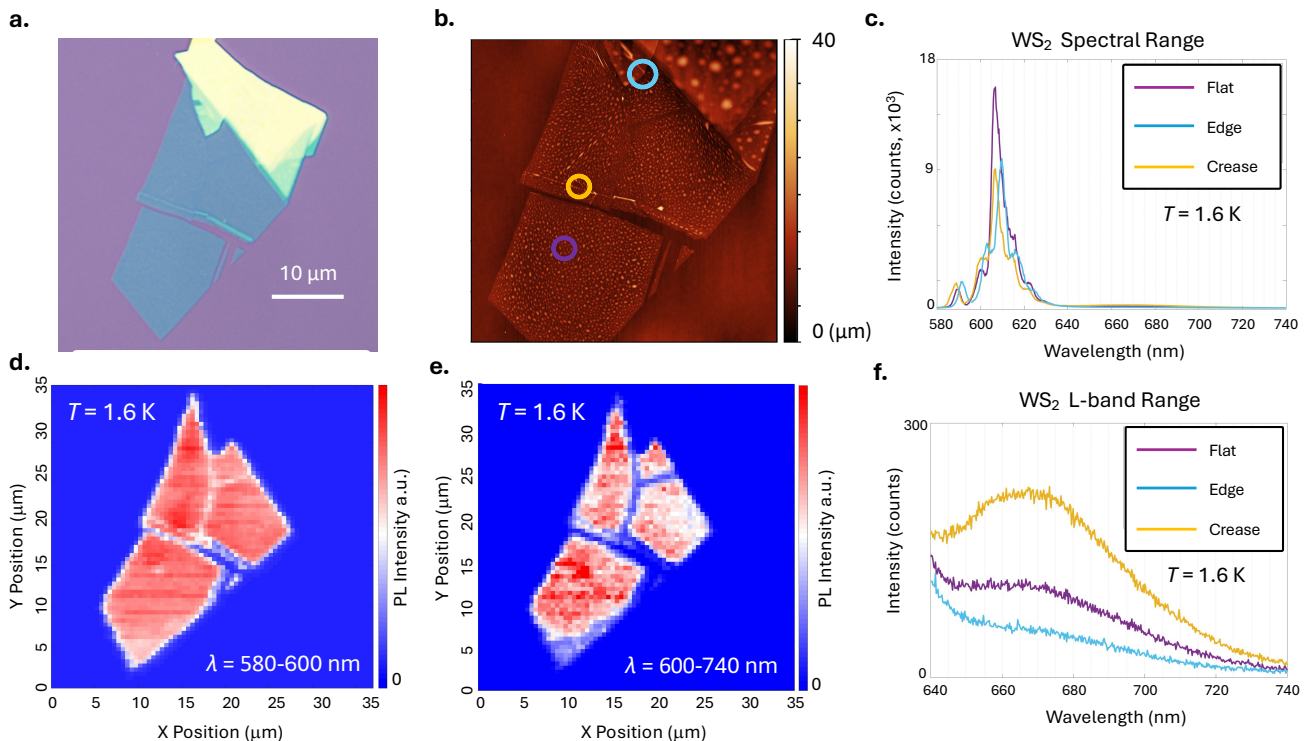


FIG. 5. (a) Optical microscope image of WS<sub>2</sub> monolayer. (b) AFM image of the WS<sub>2</sub> monolayer with flat (purple), creased (orange), and edge (blue) areas highlighted. (c) Low-temperature emission spectra from regions of WS<sub>2</sub> identified in AFM image. Variation in PL intensity is attributed to the trion peak at 606 nm. (d) Map of monolayer emission integrated over the neutral exciton range (580 – 600 nm), showing the uniform intensity of exciton emission across the flake. (e) Map of monolayer emission integrated over wavelengths beyond the neutral exciton (> 600 nm), showing a uniform intensity with no localized emission on edges and areas of strain. (f) Spectra in the defect emission range show varying intensity between flat and strained locations. Areas of high strain on WS<sub>2</sub> inferred from AFM correspond to increased L-band intensity but no localized emission features.

have a defect density far above the normal range. Spatial variation of emission in Ar-WS<sub>2</sub> is explored using PL mapping under the same conditions as the pristine materials. Figures 7a,b show a large ( $\sim 60 \mu\text{m} \times 60 \mu\text{m}$ ) monolayer area of Ar-WS<sub>2</sub> with emission roughly uniform in both total counts and peak height across the monolayer. Small regions of relatively higher intensity near the monolayer edges originate from increased defect band emission intensity (Figure 6c). The defect band is weakest on smooth areas, slightly increased on edges, and most intense on highly strained creases, similar to pristine WS<sub>2</sub> (Figure 5f). Even with the higher defect density in Ar-WS<sub>2</sub>, SPE is not observed.

#### IV. DISCUSSION

The abundant work demonstrating quantum emission from defects in WSe<sub>2</sub> compared to the relative scarcity of SPE reported in other TMDs is an unexplained problem for understanding the relationship between chalcogen vacancies and the origins of quantum emission in these

materials. Given this distinct behavior observed both in the literature and systematically identified here, a robust mechanistic explanation of SPE in tungsten TMDs should meet three primary requirements: (1) the defects responsible for SPE should be energetically preferred and abundant in typical WSe<sub>2</sub> monolayers; (2) the responsible defects should result in highly localized, radiative transitions in the band structure, and (3) the mechanism should tell a consistent story when the explanation is translated to other materials in the same family that have distinct SPE behavior.

Addressing the first and second requirements, our work isolates *vacancy configuration* as the variable for understanding how SPE forms within WSe<sub>2</sub>. The modeling results show the key difference in the band structure between the vacancy configurations is from the strongly interacting  $p_z$  character of in the divacancy configuration V2-V. A defect-centered transition is facilitated by the extended  $p_z$  orbitals of the vacancy sites. Where the in-phase delocalization of  $x$ - and  $y$ -oriented atomic orbitals in other configurations prevents radiative decay between defect states, V2-V allows the  $p_z$  state to interact, creat-

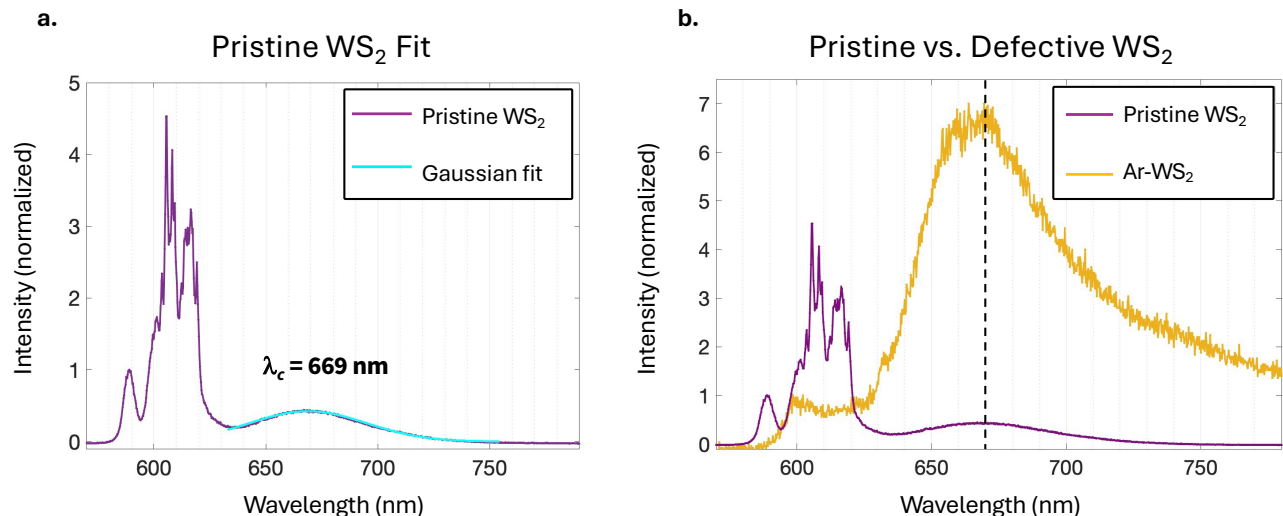


FIG. 6. Comparison of optical signatures between pristine  $\text{WS}_2$  and Ar- $\text{WS}_2$ . (a) A single gaussian peak fit (blue) of the L-band emission of pristine monolayer  $\text{WS}_2$  yields a defect emission center of  $\lambda_c = 669$  nm. (b) Comparison of L-band emission from monolayer Ar- $\text{WS}_2$  to pristine material shows an enhanced defect feature centered around 669 nm (dashed black line). Additionally, a lower energy defect band emerges in Ar- $\text{WS}_2$  that is not present on pristine material and is attributed to new divacancy formation.

ing radiative transitions between defect states. Furthermore, experimentally abundant SPE in  $\text{WSe}_2$  must come about from a naturally occurring and abundant defect. By comparing the formation energy of all the nearest neighbor vacancy configurations, V2-V is shown to be energetically preferred in the lattice over all other divacancies and closely spaced monovacancies. Collectively, this is strong evidence for the origin of SPE in  $\text{WSe}_2$ .

Addressing the third requirement, this work contextualizes the findings of  $\text{WSe}_2$  by isolating *chalcogen type* as the variable for understanding differences in SPE formation between  $\text{WSe}_2$  and  $\text{WS}_2$ . The V2-V configuration does not have the same qualitative effect on  $\text{WS}_2$  energy structure as it does in  $\text{WSe}_2$  because of the relatively small  $p_z$  orbitals in sulfur compared to selenium. This is a critical consideration for understanding how localized emitters form with differing prevalence across various TMDs. Experimentally,  $\text{WS}_2$  is characterized by L-band defect emission, and although argon plasma leads to an increased defect density and a more intense L-band, it does not translate to observing SPE in  $\text{WS}_2$ . While this is not direct experimental evidence to explain how SPE can or cannot form in  $\text{WS}_2$ , it is entirely consistent with the defect configuration picture of SPE presented here for  $\text{WSe}_2$ . In fact, this picture creates a coherent framework for understanding the emergence of SPE in both the tungsten-based TMDs. Exfoliated  $\text{WSe}_2$  exhibits SPE, whereas equivalently prepared  $\text{WS}_2$  does not. In  $\text{WSe}_2$ , vertical divacancies are likely to form where defect density is high, and those divacancies uniquely modify the band structure to give rise to highly localized de-

fect states with direct band gaps amenable to radiative emission. In  $\text{WS}_2$ , these conditions conducive to SPE are not predicted by modeling, and SPE observed neither in as-exfoliated nor high defect density materials. The fortuitous energy alignment of the V2-V defect in  $\text{WSe}_2$  is the ingredient that makes SPE uniquely prevalent in this TMD.

This work is also consistent with existing literature studying defects in TMDs. It supports the idea that monovacancies in  $\text{WSe}_2$  more readily form divacancies than in  $\text{WS}_2$  as proposed by Jeong *et al.* [42]. The conclusions here also translate to prior results for molybdenum TMDs. For example, L-band emission in  $\text{MoS}_2$  is attributed to sulfur vacancies [34], and SPE in  $\text{MoS}_2$  has only been observed after high energy irradiation from helium ions [32] or ultra-violet photons [31]. The irradiation is energetic enough to create defects with very high formation energies, such as transition metal vacancies, that would not occur in as-exfoliated material, much like in  $\text{WS}_2$ . Additionally, existing results for both  $\text{MoS}_2$  and  $\text{MoSe}_2$  suggest that quantum emission does not rely upon dark, spin-forbidden transitions since the lowest-lying energetic transition in molybdenum TMDs is spin-available [30]. The methods here are well-suited for extension to comparing between  $\text{MoS}_2$  and  $\text{MoSe}_2$  as the role of strain is ignored in favor of discovering conditions that are highly localized and radiative, independent of dark state hybridization. All together, this work offers a new framework in which to understand quantum emission in  $\text{WSe}_2$  and its unique place among the TMDs.



## AUTHOR CONTRIBUTIONS

S.C.G. conceptualized the work and performed optical spectroscopy and photon counting. C.J.Z performed first principles calculations. S.C.G. and C.J.Z together analyzed and interpreted results. A.D. and Y.L. prepared and characterized pristine materials. W.W. prepared defect-engineered material. S.C.G. and C.J.Z. prepared the manuscript with contributions from all authors. N.P.S., G.C.S., M.C.H., T.J.M. and S.H. supervised the project.

## COMPETING INTERESTS

The authors declare no competing interests.

## ACKNOWLEDGMENTS

This work was primarily supported by the Center for Molecular Quantum Transduction, an Energy Frontier Research Center funded by the U.S. Department of Energy, Office of Science, Office of Basic Energy Sciences, under Award No. DE-SC0021314. Partial support was also provided for the preparation of pristine materials by the National Science Foundation Materials Research Science and Engineering Center at Northwestern University under Award No. DMR-2308691. W.W. and S.H. acknowledge the support from the National Science Foundation (Grant No. ECCS-2246564, ECCS-1943895), the Air Force Office of Scientific Research (AFOSR, Grant No. FA9550-22-1-0408), and the Robert A. Welch Foundation (Grant No. C-2144). S.C.G. gratefully acknowledges Jash Jain for writing Python code to efficiently analyze spectral data.

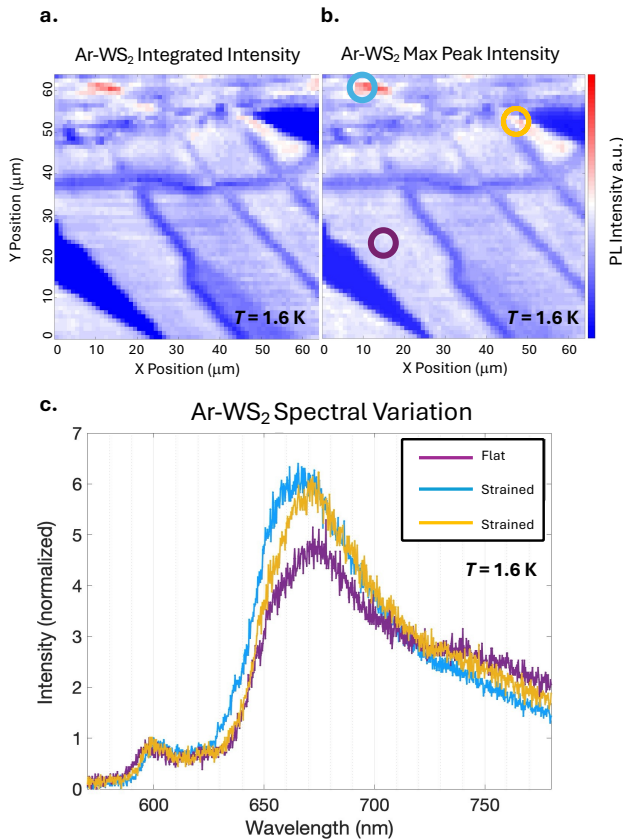


FIG. 7. (a) Map of integrated emission intensity from Ar-WS<sub>2</sub>. (b) Map of the same area in (a) but plotting peak intensity. (c) Selected spectra from Ar-WS<sub>2</sub> show how map intensity variations correspond to a roughly 20% increase in the monovacancy defect band between areas of strain (blue and orange) and flat monolayer (purple), but without localized emission peaks.

- 
- [1] S. Gupta, W. Wu, S. Huang, and B. I. Yakobson, Single-photon emission from two-dimensional materials, to a brighter future, *The Journal of Physical Chemistry Letters* **14**, 3274 (2023).
- [2] I. Aharonovich, D. Englund, and M. Toth, Solid-state single-photon emitters, *Nature Photonics* **10**, 631 (2016).
- [3] A. B. D.-a.-j.-w.-i. Shaik and P. Palla, Optical quantum technologies with hexagonal boron nitride single photon sources, *Scientific Reports* **11**, 12285 (2021).
- [4] S. Manzeli, D. Ovchinnikov, D. Pasquier, O. V. Yazyev, and A. Kis, 2D transition metal dichalcogenides, *Nature Reviews Materials* **2**, 1 (2017).
- [5] Y. Liu, Y. Gao, S. Zhang, J. He, J. Yu, and Z. Liu, Valleytronics in transition metal dichalcogenides materials, *Nano Research* **12**, 2695 (2019).
- [6] M. I. B. Utama, H. Zeng, T. Sadhukhan, A. Dasgupta, S. C. Gavin, R. Ananth, D. Lebedev, W. Wang, J.-S. Chen, K. Watanabe, *et al.*, Chemomechanical modification of quantum emission in monolayer WSe<sub>2</sub>, *Nature Communications* **14**, 2193 (2023).
- [7] H.-J. Chuang, C. E. Stevens, M. R. Rosenberger, S.-J. Lee, K. M. McCreary, J. R. Hendrickson, and B. T. Jonker, Enhancing single photon emission purity via design of van der waals heterostructures, *Nano Letters* (2024).
- [8] P. Tonndorf, R. Schmidt, R. Schneider, J. Kern, M. Buscema, G. A. Steele, A. Castellanos-Gomez, H. S. van der Zant, S. M. de Vasconcellos, and R. Bratschkitsch, Single-photon emission from localized excitons in an atomically thin semiconductor, *Optica* **2**, 347 (2015).
- [9] M. Koperski, K. Nogajewski, A. Arora, V. Cherkez, P. Mallet, J.-Y. Veuillen, J. Marcus, P. Kossacki, and M. Potemski, Single photon emitters in exfoliated WSe<sub>2</sub> structures, *Nature Nanotechnology* **10**, 503 (2015).

- [10] Y.-M. He, G. Clark, J. R. Schaibley, Y. He, M.-C. Chen, Y.-J. Wei, X. Ding, Q. Zhang, W. Yao, X. Xu, *et al.*, Single quantum emitters in monolayer semiconductors, *Nature Nanotechnology* **10**, 497 (2015).
- [11] A. Srivastava, M. Sidler, A. V. Allain, D. S. Lembke, A. Kis, and A. Imamoglu, Optically active quantum dots in monolayer WSe<sub>2</sub>, *Nature Nanotechnology* **10**, 491 (2015).
- [12] S. Tongay, J. Suh, C. Ataca, W. Fan, A. Luce, J. S. Kang, J. Liu, C. Ko, R. Raghunathanan, J. Zhou, *et al.*, Defects activated photoluminescence in two-dimensional semiconductors: interplay between bound, charged and free excitons, *Scientific Reports* **3**, 2657 (2013).
- [13] A. Srivastava, M. Sidler, A. V. Allain, D. S. Lembke, A. Kis, and A. Imamoglu, Optically active quantum dots in monolayer WSe<sub>2</sub>, *Nature Nanotechnology* **10**, 491 (2015).
- [14] K. Thakar and S. Lodha, Optoelectronic and photonic devices based on transition metal dichalcogenides, *Materials Research Express* **7**, 014002 (2020).
- [15] S. Kim, All-2D material photonic devices, *Nanoscale Advances* **5**, 323 (2023).
- [16] E. J. Lenferink, T. LaMountain, T. K. Stanev, E. Garvey, K. Watanabe, T. Taniguchi, and N. P. Stern, Tunable emission from localized excitons deterministically positioned in monolayer p-n junctions, *ACS Photonics* **9**, 3067 (2022).
- [17] S. Schwarz, A. Kozikov, F. Withers, J. Maguire, A. Foster, S. Dufferwiel, L. Hague, M. Makhonin, L. Wilson, A. Geim, *et al.*, Electrically pumped single-defect light emitters in WSe<sub>2</sub>, *2D Materials* **3**, 025038 (2016).
- [18] G. Clark, J. R. Schaibley, J. Ross, T. Taniguchi, K. Watanabe, J. R. Hendrickson, S. Mou, W. Yao, and X. Xu, Single defect light-emitting diode in a van der waals heterostructure, *Nano Letters* **16**, 3944 (2016).
- [19] C. Palacios-Berraquero, Atomically-thin quantum light emitting diodes, *Quantum Confined Excitons in 2-dimensional Materials*, 71 (2018).
- [20] A. Branny, S. Kumar, R. Proux, and B. D. Gerardot, Deterministic strain-induced arrays of quantum emitters in a two-dimensional semiconductor, *Nature Communications* **8**, 15053 (2017).
- [21] L. Sortino, P. G. Zotev, C. L. Phillips, A. J. Brash, J. Cambiasso, E. Marensi, A. M. Fox, S. A. Maier, R. Sapienza, and A. I. Tartakovskii, Bright single photon emitters with enhanced quantum efficiency in a two-dimensional semiconductor coupled with dielectric nano-antennas, *Nature Communications* **12**, 6063 (2021).
- [22] C. E. Stevens, H.-J. Chuang, M. R. Rosenberger, K. M. McCreary, C. K. Dass, B. T. Jonker, and J. R. Hendrickson, Enhancing the purity of deterministically placed quantum emitters in monolayer WSe<sub>2</sub>, *ACS Nano* **16**, 20956 (2022).
- [23] K. Parto, S. I. Azzam, K. Banerjee, and G. Moody, Defect and strain engineering of monolayer WSe<sub>2</sub> enables site-controlled single-photon emission up to 150 K, *Nature Communications* **12**, 3585 (2021).
- [24] Z. Cui, X. Ke, E. Li, X. Wang, Y. Ding, T. Liu, M. Li, and B. Zhao, Effect of vacancy defect on optoelectronic properties of monolayer tungsten diselenide, *Optical and Quantum Electronics* **50**, 1 (2018).
- [25] P. Kapuściński, A. Delhomme, D. Vaclavkova, A. O. Slobodeniuk, M. Grzeszczyk, M. Bartos, K. Watanabe, T. Taniguchi, C. Faugeras, and M. Potemski, Rydberg series of dark excitons and the conduction band spin-orbit splitting in monolayer WSe<sub>2</sub>, *Communications Physics* **4**, 186 (2021).
- [26] P. Hernández López, S. Heeg, C. Schattauer, S. Kovalchuk, A. Kumar, D. J. Bock, J. N. Kirchhof, B. Höfer, K. Greben, D. Yagodkin, *et al.*, Strain control of hybridization between dark and localized excitons in a 2D semiconductor, *Nature Communications* **13**, 7691 (2022).
- [27] Y. J. Zheng, Y. Chen, Y. L. Huang, P. K. Gogoi, M.-Y. Li, L.-J. Li, P. E. Trevisanutto, Q. Wang, S. J. Pennycook, A. T. Wee, *et al.*, Point defects and localized excitons in 2d WSe<sub>2</sub>, *ACS Nano* **13**, 6050 (2019).
- [28] S. Zhang, C.-G. Wang, M.-Y. Li, D. Huang, L.-J. Li, W. Ji, and S. Wu, Defect structure of localized excitons in a WSe<sub>2</sub> monolayer, *Physical Review Letters* **119**, 046101 (2017).
- [29] K. Ko, M. Jang, J. Kwon, and J. Suh, Native point defects in 2D transition metal dichalcogenides: A perspective bridging intrinsic physical properties and device applications, *Journal of Applied Physics* **135** (2024).
- [30] L. Yu, M. Deng, J. L. Zhang, S. Borghardt, B. Kardynal, J. Vuckovic, and T. F. Heinz, Site-controlled quantum emitters in monolayer MoSe<sub>2</sub>, *Nano Letters* **21**, 2376 (2021).
- [31] W. Wang, L. O. Jones, J.-S. Chen, G. C. Schatz, and X. Ma, Utilizing ultraviolet photons to generate single-photon emitters in semiconductor monolayers, *ACS Nano* **16**, 21240 (2022).
- [32] J. Klein, M. Lorke, M. Florian, F. Sigger, L. Sigl, S. Rey, J. Wierzbowski, J. Cerne, K. Müller, E. Mitterreiter, *et al.*, Site-selectively generated photon emitters in monolayer MoS<sub>2</sub> via local helium ion irradiation, *Nature Communications* **10**, 2755 (2019).
- [33] P. K. Chow, R. B. Jacobs-Gedrim, J. Gao, T.-M. Lu, B. Yu, H. Terrones, and N. Koratkar, Defect-induced photoluminescence in monolayer semiconducting transition metal dichalcogenides, *ACS Nano* **9**, 1520 (2015).
- [34] T. Verhagen, V. L. Guerra, G. Haider, M. Kalbac, and J. Vejpravova, Towards the evaluation of defects in MoS<sub>2</sub> using cryogenic photoluminescence spectroscopy, *Nanoscale* **12**, 3019 (2020).
- [35] S. Cianci, E. Blundo, F. Tuzi, G. Pettinari, K. Olkowska-Pucko, E. Parmenopoulou, D. B. Peeters, A. Miriametro, T. Taniguchi, K. Watanabe, *et al.*, Spatially controlled single photon emitters in hBN-capped WS<sub>2</sub> domes, *Advanced Optical Materials* **11**, 2202953 (2023).
- [36] D. Bao, A. G. Del Águila, T. T. H. Do, S. Liu, J. Pei, and Q. Xiong, Probing momentum-indirect excitons by near-resonance photoluminescence excitation spectroscopy in WS<sub>2</sub> monolayer, *2D Materials* **7**, 031002 (2020).
- [37] R. H. Godiksen, S. Wang, T. Raziman, J. G. Rivas, and A. G. Curto, Impact of indirect transitions on valley polarization in WS<sub>2</sub> and WSe<sub>2</sub>, *Nanoscale* **14**, 17761 (2022).
- [38] T. Verhagen, V. L. Guerra, G. Haider, M. Kalbac, and J. Vejpravova, Towards the evaluation of defects in MoS<sub>2</sub> using cryogenic photoluminescence spectroscopy, *Nanoscale* **12**, 3019 (2020).

- [39] F. Aryeetey, T. Ignatova, and S. Aravamudhan, Quantification of defects engineered in single layer MoS<sub>2</sub>, *RSC Advances* **10**, 22996 (2020).
- [40] D. Liu, Y. Guo, L. Fang, and J. Robertson, Sulfur vacancies in monolayer MoS<sub>2</sub> and its electrical contacts, *Applied Physics Letters* **103** (2013).
- [41] W. Zhou, X. Zou, S. Najmaei, Z. Liu, Y. Shi, J. Kong, J. Lou, P. M. Ajayan, B. I. Yakobson, and J.-C. Idrobo, Intrinsic structural defects in monolayer molybdenum disulfide, *Nano Letters* **13**, 2615 (2013).
- [42] T. Y. Jeong, H. Kim, S.-J. Choi, K. Watanabe, T. Taniguchi, K. J. Yee, Y.-S. Kim, and S. Jung, Spectroscopic studies of atomic defects and bandgap renormalization in semiconducting monolayer transition metal dichalcogenides, *Nature Communications* **10**, 3825 (2019).
- [43] T. Sadhukhan and G. C. Schatz, Generating bright emissive states by modulating the bandgap of monolayer tungsten diselenide, *The Journal of Physical Chemistry C* **126**, 5598 (2022).
- [44] J. Heyd, J. E. Peralta, G. E. Scuseria, and R. L. Martin, Energy band gaps and lattice parameters evaluated with the heyd-scuseria-ernzerhof screened hybrid functional, *The Journal of Chemical Physics* **123** (2005).
- [45] J. E. Moussa, P. A. Schultz, and J. R. Chelikowsky, Analysis of the heyd-scuseria-ernzerhof density functional parameter space, *The Journal of Chemical Physics* **136** (2012).
- [46] S. Khalid, B. Medasani, J. L. Lyons, D. Wickramaratne, and A. Janotti, The deep-acceptor nature of the chalcogen vacancies in 2D transition-metal dichalcogenides, *2D Materials* **11**, 021001 (2024).
- [47] Y. Sun, D. Wang, and Z. Shuai, Indirect-to-direct band gap crossover in few-layer transition metal dichalcogenides: a theoretical prediction, *The Journal of Physical Chemistry C* **120**, 21866 (2016).
- [48] C.-x. Yang, X. Zhao, and S.-y. Wei, Manipulation of electronic structure in wse<sub>2</sub> monolayer by strain, *Solid State Communications* **245**, 70 (2016).
- [49] J. Shang, X. Shen, C. Cong, N. Peimyoo, B. Cao, M. Eginligil, and T. Yu, Observation of excitonic fine structure in a 2D transition-metal dichalcogenide semiconductor, *ACS Nano* **9**, 647 (2015).
- [50] M. A. Aly, M. Shah, L. M. Schneider, K. Kang, M. Koch, E.-H. Yang, and A. Rahimi-Iman, Radiative pattern of intralayer and interlayer excitons in two-dimensional WS<sub>2</sub>/WSe<sub>2</sub> heterostructure, *Scientific Reports* **12**, 6939 (2022).
- [51] M. Groll, J. Bürger, I. Caltzidis, K. D. Jöns, W. G. Schmidt, U. Gerstmann, and J. K. Lindner, Dft-assisted investigation of the electric field and charge density distribution of pristine and defective 2d wse<sub>2</sub> by differential phase contrast imaging, *Small*, 2311635 (2024).
- [52] L. Fang, H. Chen, X. Yuan, H. Huang, G. Chen, L. Li, J. Ding, J. He, and S. Tao, Quick optical identification of the defect formation in monolayer WSe<sub>2</sub> for growth optimization, *Nanoscale Research Letters* **14**, 1 (2019).
- [53] M. Aghajanian, A. A. Mostofi, and J. Lischner, Optical properties of charged defects in monolayer MoS<sub>2</sub>, *Electronic Structure* **5**, 045012 (2023).
- [54] M. R. Molas, K. Nogajewski, A. O. Slobodeniuk, J. Binder, M. Bartos, and M. Potemski, The optical response of monolayer, few-layer and bulk tungsten disulfide, *Nanoscale* **9**, 13128 (2017).
- [55] M. Zinkiewicz, A. Slobodeniuk, T. Kazimierczuk, P. Kapuściński, K. Oreszczuk, M. Grzeszczyk, M. Bartos, K. Nogajewski, K. Watanabe, T. Taniguchi, *et al.*, Neutral and charged dark excitons in monolayer WS<sub>2</sub>, *Nanoscale* **12**, 18153 (2020).
- [56] E. Mitterreiter, B. Schuler, A. Micevic, D. Hernangómez-Pérez, K. Barthelmi, K. A. Cochrane, J. Kiemle, F. Sigger, J. Klein, E. Wong, *et al.*, The role of chalcogen vacancies for atomic defect emission in MoS<sub>2</sub>, *Nature Communications* **12**, 3822 (2021).
- [57] Q. Qian, W. Wu, L. Peng, Y. Wang, A. M. Z. Tan, L. Liang, S. M. Hus, K. Wang, T. H. Choudhury, J. M. Redwing, *et al.*, Photoluminescence induced by substitutional nitrogen in single-layer tungsten disulfide, *ACS Nano* **16**, 7428 (2022).
- [58] Z. He, X. Wang, W. Xu, Y. Zhou, Y. Sheng, Y. Rong, J. M. Smith, and J. H. Warner, Revealing defect-state photoluminescence in monolayer WS<sub>2</sub> by cryogenic laser processing, *ACS Nano* **10**, 5847 (2016).
- [59] A. Castellanos-Gomez, M. Buscema, R. Molenaar, V. Singh, L. Janssen, H. S. Van Der Zant, and G. A. Steele, Deterministic transfer of two-dimensional materials by all-dry viscoelastic stamping, *2D Materials* **1**, 011002 (2014).
- [60] F. Liu, W. Wu, Y. Bai, S. H. Chae, Q. Li, J. Wang, J. Hone, and X.-Y. Zhu, Disassembling 2D van der waals crystals into macroscopic monolayers and reassembling into artificial lattices, *Science* **367**, 903 (2020).

## Appendix A: Sample Preparation and Characterization

Pristine monolayer  $\text{WS}_2$  and  $\text{WSe}_2$  were exfoliated from a bulk crystal (2D Semiconductors) via micromechanical exfoliation and then transferred onto Si/SiO<sub>2</sub> substrates using a dry viscoelastic stamping method [59]. AFM images were obtained in ambient conditions (Asylum Cypher S in tapping mode, NCHR-W Pointprobe tips). Ar- $\text{WS}_2$  was made by mechanically exfoliating  $\text{WS}_2$  using a gold-tape assisted method [60] before being bombarded with argon plasma. Because the exfoliation methods were varied between pristine  $\text{WS}_2$  and Ar- $\text{WS}_2$ , the optical properties of each were measured to ensure that any observed spectroscopic differences were due to plasma and not to exfoliation. Figure 8a shows a PL map of gold tape exfoliated  $\text{WS}_2$  and Figure 8b shows selected spectra from areas of high intensity. These results are consistent with pristine material, which shows a uniformity in exciton emission across the monolayer area and small areas of increased intensity owing to a dominant trion [54, 55].

We also note that making conclusions about Ar- $\text{WS}_2$  relies on the assumption that the engineered defects are preserved and unpassivated after application of argon plasma. Therefore, to ensure that the defects remained unpassivated from environmental adsorbates for spectroscopic measurements, the Ar- $\text{WS}_2$  was sealed inside an air-free glove box and transported under vacuum inside a container made from a KF-25 to KF-16 conical reducer and corresponding O-rings and clamps.

## Appendix B: Low Temperature Optical Spectroscopy

Cryogenic measurements were performed in an AttoDry 2100 cryostat at 1.6 K; high-resolution spatial mapping was achieved using Attocube piezoelectric nanopositioners in the  $x - y$  plane within the cryostat. Confocal spectroscopy was performed using a 0.82 NA, 100 $\times$  magnification objective that focused a 532 nm diode laser onto the sample. The diffraction-limited spot size is estimated to be  $D = 1.22\lambda/NA \approx 0.79 \mu\text{m}$ . Light was collected with an optical fiber and sent to a 750-mm focal length spectrometer (Andor Shamrock SR-750) with a thermoelectrically-cooled CCD camera (DU420A-BEX2-DD). A Hanbury Brown-Twiss setup was used to measure the coherence. Signals were sent into an optical fiber that then splits via a 1  $\times$  2 fiber splitter to direct equal signals to two avalanche photodiodes (APD; PicoQuant,  $\tau$ -SPAD-100). To isolate light from the emitter of interest, a 10 nm FWHM bandpass filter of the appropriate center wavelength was used. The raw photon coincidence data was used to calculate the second-order intensity correlation function  $g^{(2)}(\tau)$ . Background correction was applied to extract the final  $g^{(2)}(0)$  value. The correction only accounts for the background arising from dark counts on the APD from light contamination of the measurement environment. The background count rate was obtained from the APD with laser illumination blocked. For each SPE source presented in this work, the background correction did not alter the extracted  $g^{(2)}(0)$  value. Three distinct localized emitter sites from monolayer  $\text{WSe}_2$  were characterized with second order correlation measurements; in addition to the emitter highlighted in main text (green), two are shown in Figure 9.

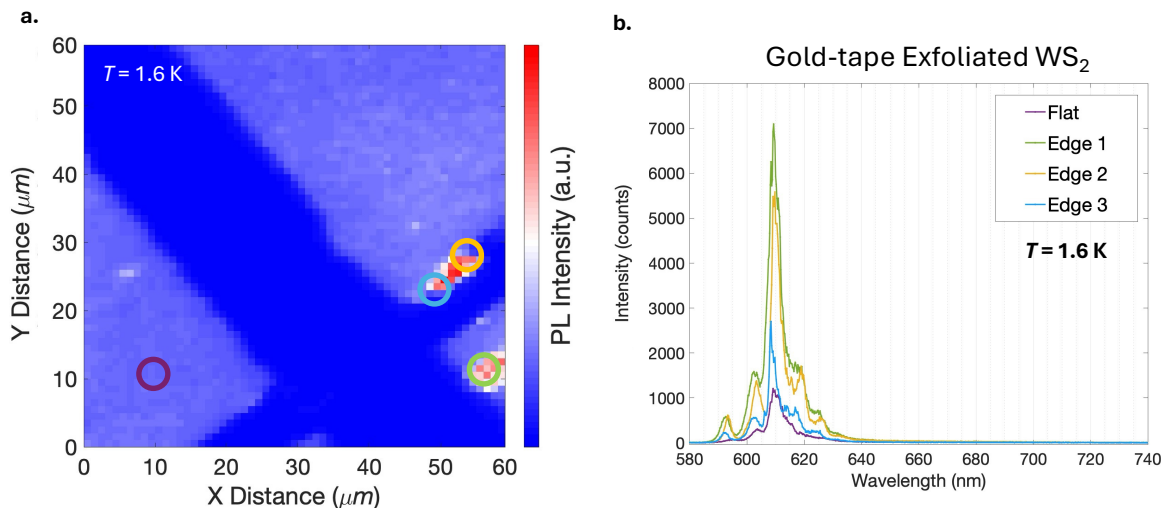


FIG. 8. (a) PL map of gold-exfoliated  $\text{WS}_2$  with a small area of increased intensity on one edge. (b) Selected spectra from different locations showing that the increased intensity is primarily due to  $\sim 7\times$  increase in the dominant trion emission at 609 nm, consistent with scotch tape exfoliated material.

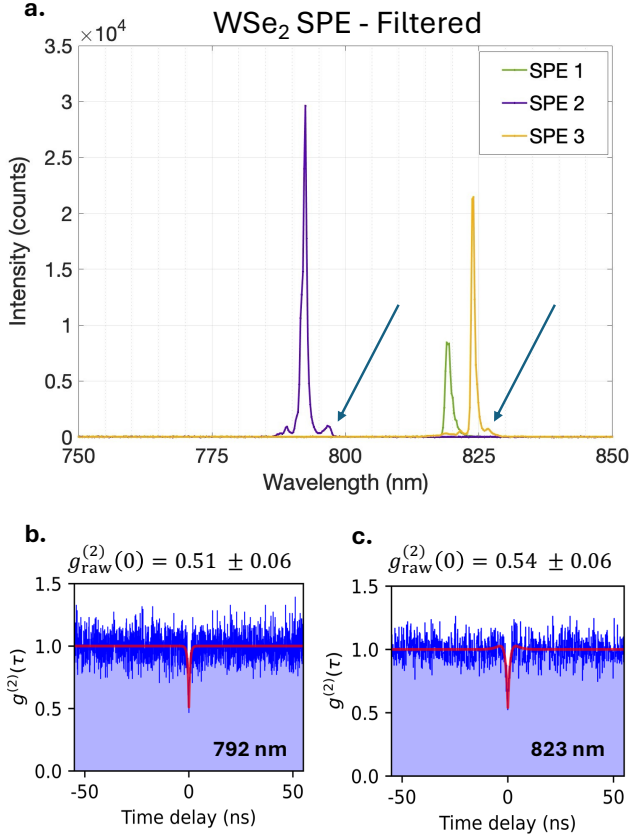


FIG. 9. (a) Spectra of three emitter sites identified as SPE from  $\text{WSe}_2$ . These spectra show the emission lines filtered as they were for photon counting. Arrows indicate spectral contamination that could not be filtered out for measurement, accounting for higher  $g^2(0)$  values, shown in (b) and (c).

### Appendix C: Computation

All calculations were performed in the Vienna Ab Initio Simulation Package (VASP, v. 5.4.4) using a  $3 \times 3 \times 1.5$  supercell for both  $\text{WSe}_2$  and  $\text{WS}_2$  with a  $20 \text{ \AA}$  vacuum space introduced in the  $z$ -direction to simulate a surface. Pseudopotentials with a frozen core are included to give six explicit electrons for W, S, and Se. Preliminarily, geometry optimization of the atomic coordinates and  $x, y$  lattice vectors for each pristine supercell was done using a  $4 \times 4 \times 1$  Monkhorst-Pack mesh of  $k$ -points with a convergence tolerance of  $F_{\text{max}} < 0.01 \text{ eV/\AA}$  without symmetry constraint. This corresponds to an average of 1 to 2 chalcogenide vacancies per supercell. Atomic coordinates for single vacancies and each possible divacancy configuration were then optimized at the same level of theory while constraining lattice vectors. It is noted that a pristine unit cell of TMDs is typically presented as a direct

bandgap semiconductor that is K-centered. However in these calculations, the space group is altered such that the direct bandgap is now  $\Gamma$ -centered and is a remnant of the supercell construction but does not alter the physical meaning of the result. Band structures for all divacancy configurations are shown in Figures 10 and 11.

Vacancy formation energies  $E_f^q$  were determined using the following equation:

$$E_f^q = E_{\text{tot}}^{\text{def}} - E_{\text{tot}}^{\text{bulk}} - \sum_i n_i \mu_i + q(E_f + E_{\text{VBM}}) \quad (\text{C1})$$

The first two terms give the total energy difference between the pristine supercell and the defected supercell. The value  $\mu_i$  is the chemical potential of the chalcogenide, taken from a single-point energy of the bulk material, and  $n_i$  is the quantity of that atom type removed from the supercell. The charge of the defect,  $q$ , is equal to 0 in all cases. To determine chemical potentials, octathiocane in the gas phase was used for sulfur and the trigonal (grey) allotrope for selenium at the same level of theory. Formation energies of all configurations are shown in Table I.

Vacancy Configuration	Energy (eV)	Formation Energy $E_f^0$ (eV)
<b><math>\text{WS}_2</math></b>		
V1	-265.693	3.158
V2-V	-256.089	6.216
V2-A	-255.875	6.430
V2-B	-255.823	6.482
V2-C	-255.872	6.433
V2-D	-255.939	6.366
<b><math>\text{WSe}_2</math></b>		
V1	-240.667	2.977
V2-V	-232.663	5.539
V2-A	-232.116	6.086
V2-B	-231.994	6.208
V2-C	-232.082	6.120
V2-D	-232.187	6.015

TABLE I. Formation energies of modeled vacancy configurations.

WSe<sub>2</sub>

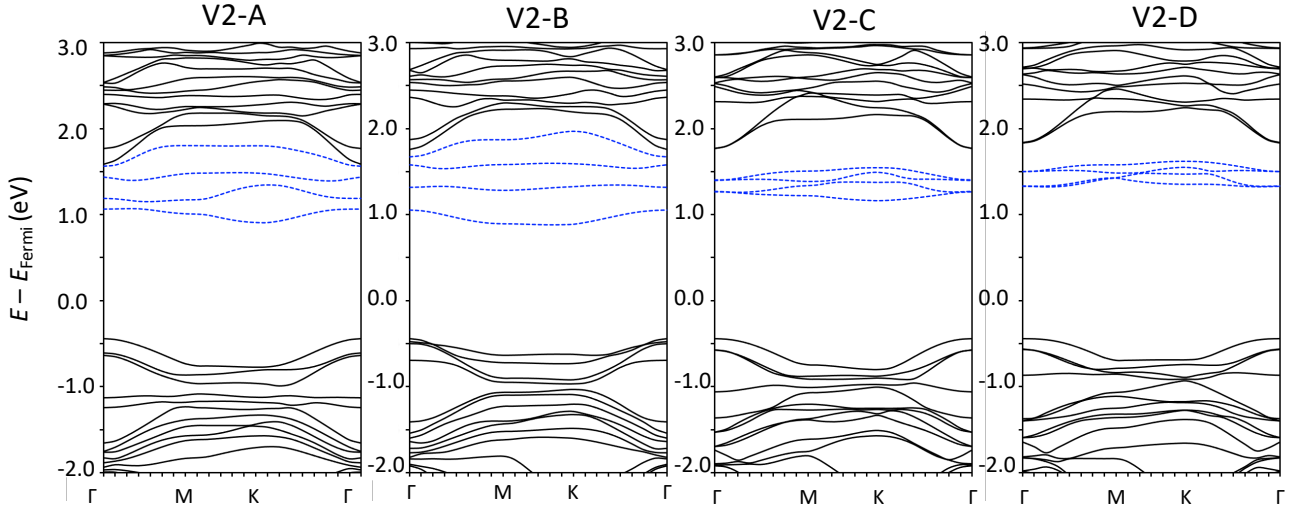


FIG. 10. Band structures of bivacancy defect formations V2-A, V2-B, V2-C, V2-D for WSe<sub>2</sub>.

WS<sub>2</sub>

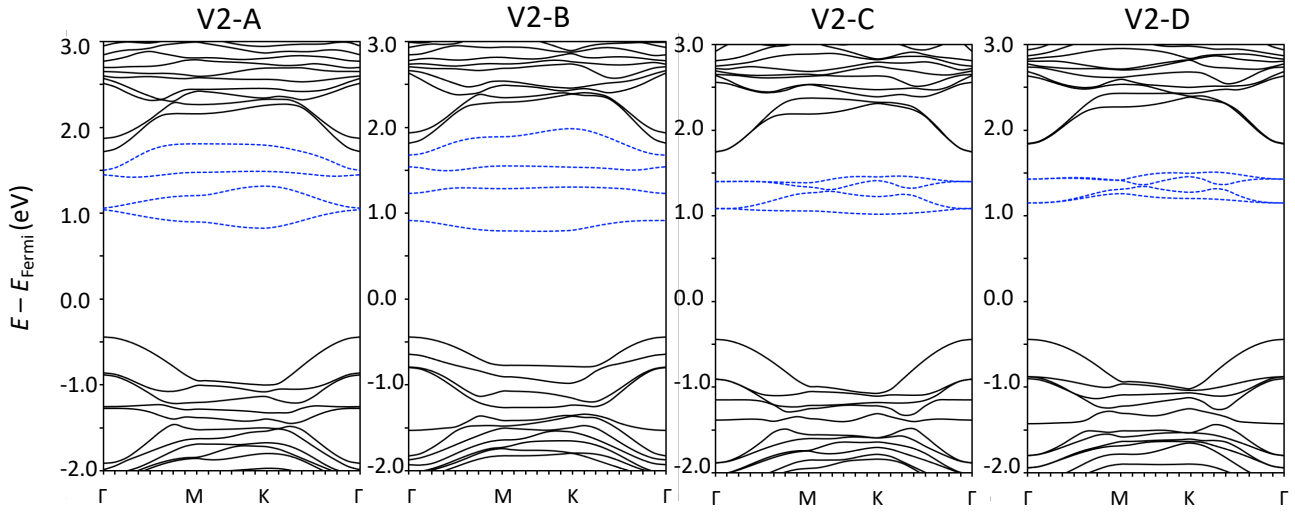


FIG. 11. Band structures of bivacancy defect formations V2-A, V2-B, V2-C, V2-D for WS<sub>2</sub>.